Unveiling microbial single-cell growth dynamics under rapid periodic oxygen oscillations

Keitaro Kasahara[1,2]**, Johannes Seiffarth**[1,2]**, Birgit Stute**[1]**, Eric von Lieres**[1,2]**, Thomas Drepper**[3]**, Katharina Nöh**[1]**, and Dietrich Kohlheyer**[1,*]

[1]IBG-1: Biotechnology, Institute of Bio- and Geosciences, Forschungszentrum Jülich GmbH, Jülich, Germany

[2]Computational Systems Biotechnology (AVT.CSB), RWTH Aachen University, Aachen, Germany

[3]Institute of Molecular Enzyme Technology, Heinrich Heine University Düsseldorf, Forschungszentrum Jülich GmbH, Jülich, Germany

[*]Corresponding author: *IBG-1: Biotechnology, Institute of Bio- and Geosciences, Forschungszentrum Jülich GmbH, 52425 Jülich, Germany. Email: d.kohlheyer@fz-juelich.de*

ABSTRACT

Microbial metabolism and growth are tightly linked to oxygen (O_2). Microbes experience fluctuating O_2 levels in natural environments; however, our understanding of how cells respond to fluctuating O_2 over various time scales remains limited, due to challenges in observing microbial growth at single-cell resolution under controlled O_2 conditions and in linking individual cell growth with the specific O_2 microenvironment. We performed time-resolved microbial growth analyses at single-cell resolution under a temporally controlled O_2 supply. A multilayer microfluidic device was developed, featuring gas supply above a cultivation layer, separated by a thin membrane enabling efficient gas transfer. This platform enables microbial cultivation under constant, dynamic, and oscillating O_2 conditions. Automated time-lapse microscopy and deep-learning-based image analysis provide access to spatiotemporally resolved growth data at the single-cell level. O_2 switching within tens of seconds, coupled with precise monitoring of the microenvironment, allows us to accurately correlate cellular growth with local O_2 concentrations. Growing *Escherichia coli* microcolonies subjected to varying O_2 oscillation periods show distinct growth dynamics, characterized by response and recovery phases. The comprehensive growth data and insights gained from our unique platform are a crucial step forward to systematically study cell response and adaptation to fluctuating O_2 environments at single-cell resolution.

Introduction

Microbes in natural habitats are exposed to external environmental changes and have evolved strategies to adapt to the surrounding conditions[1]. They proliferate in fluctuating environments on different time scales with different parameters, such as the availability of molecular oxygen (O_2)[2], nutrients[3], pH[4], temperature[5], and light[6]. These fluctuating environmental conditions are pervasive, including the ocean[3] and soil[5], as well as in animal hosts, such as in the nasal passage[4], lung[7] and intestine[8]. Fluctuating environments are also prevalent in biotechnological cultivation setups. Industrial large-scale bioreactors, for instance, stir large volumes of culture broth, often resulting in inefficient mixing and heterogeneous distribution of O_2 and nutrients, which could potentially lead to yield losses[9–11]. Investigating microbial behavior in fluctuating environments will therefore improve our understanding of microbial adaptation to external environmental changes and may offer insights into how to enhance efficiency in industrial biotechnology.

Among the various environmental conditions, the availability of O_2 is one of the most critical for microbial growth and physiology. O_2 is intricately linked with a multitude of microbial processes, including iron homeostasis[12], oxidative stress[13], the development of pathogenic infections[14] and biofilm growth[15]. In addition to these microbial processes associated with O_2 availability, O_2 is also valuable as a primary electron acceptor for aerobic respiration in many microorganisms. In particular, facultative anaerobes, which are capable of growing under both aerobic and anaerobic conditions, adapt to changing O_2 environments by switching their metabolic pathways between aerobic respiration and anaerobic respiration/fermentation[16,17]. This ability of facultative anaerobes to adapt to different O_2 environments has been extensively studied under single-shift O_2 environments. Previous studies have primarily focused on examining intracellular adaptation, such as transcriptome[16], protein synthesis[18], metabolome[19], flux balance[20], and phenotypic adaptation like growth fitness[21]. These studies have mostly been conducted in conventional cultivation setups, including microtiter plates, shaking flasks, and bioreactors. However, there is a lack of understanding regarding the cellular capability to adapt to rapidly fluctuating O_2 environments. Recent studies indicate that microbial behavior in fluctuating environments, where conditions shift within seconds to minutes, can differ significantly from behaviors observed in single-shift experiments[22,23].

Investigating the impact of O_2 fluctuations on microbial growth would facilitate a more comprehensive understanding of adaptation processes that remain to be elucidated.

The study of microbial responses to O_2 fluctuations has been hindered by several constraints. Conventional cultivation techniques do not facilitate rapid and precise changes in O_2 concentrations on the timescale of seconds to minutes, nor do they allow for simultaneous, high-resolution data acquisition. Environmental control in conventional laboratory cultivation setups is typically slow, with limited precision in maintaining homogeneity, temporal consistency, and resulting O_2 microenvironments. Additionally, these setups are often incompatible with fully resolving growth physiology under fluctuating O_2 conditions, as repetitive sampling is impractical without disrupting the culture. Consequently, it has been challenging to analyze the cellular response in terms of microbial growth and physiology caused by rapid O_2 fluctuations.

Today, microfluidic devices with precise environmental control and imaging at single-cell resolution are gaining attention as novel tools for creating oscillating environments on-chip and extracting microbial growth data with high temporal resolution. Although some microfluidic systems have been developed to mimic oscillating conditions for pH, nutrients, and O_2[23–25], detailed analysis linking microbial growth dynamics to fluctuating O_2 environments remain limited. To better understand microbial adaptation processes under rapid O_2 fluctuations, a platform is needed that allows for high-resolution, single-cell analysis of microbial growth, explicitly correlated with well-defined O_2 fluctuations (Fig. 1A).

In this work, we investigated, for the first time, the growth dynamics of the facultative anaerobe *Escherichia coli* (*E. coli*) MG1655 under O_2 oscillations occurring within minutes. To address the aforementioned limitations, we developed a double-layer microfluidic chip to facilitate rapid gas exchange within the cultivation chambers and frequent data acquisition accompanied by time-lapse microscopy to analyze cell division at the single-cell resolution (Fig. 1B). The polydimethylsiloxane (PDMS) microfluidic chip is composed of two layers, an upper layer for gassing and a lower layer with multiple chambers for microbial cultivation. A thin intermediate PDMS membrane (65 μm) separates the two layers, facilitating rapid gas diffusion from the upper to the lower layer. The performance of the microfluidic chip was evaluated by spatially resolved O_2 imaging in the fluid channel using fluorescence lifetime imaging (FLIM) microscopy and a fluorescent O_2-sensitive dye. The microfluidic chip, automated time-lapse microscopy, and following deep-learning-based image analysis compose a versatile platform to analyze microbial

growth and its correlation to applied O_2 oscillations. The platform was employed to cultivate *E. coli* under well-defined O_2 oscillating environments with varying oscillation periods, to examine cellular adaptation in a time-resolved manner. Here, we report periodically oscillating microbial growth dynamics composed of several adaptation phases and synchronized with applied O_2 oscillations.

Results

On-chip O_2 control with the double-layer chip

The double-layer chip was fabricated by molding the upper and the lower layers separately and subsequently assembling them as shown in Fig. 2A. The fabricated chip is depicted in Fig. 2B. For visualization purposes, the top gas-layer channels (red) and bottom fluid-layer channels (blue) were filled with colored dyes. The SEM image (Fig. 2B (i)) depicts a series of cultivation chambers (50 μm×30 μm×1 μm), in which cells are trapped and their growth can be observed over time via time-lapse imaging during cultivation. Each growth chamber is connected to two parallel medium supply channels ($w = 100$ μm, $h =$ 10 μm) enabling continuous medium perfusion but mass transfer inside the chamber solely by diffusion. The cross-sectional photograph of the device (Fig. 2B (ii)) shows the PDMS membrane, which has a thickness of approximately 65 μm (fluid layer in the figure), physically separating the upper gas channel from the lower fluid channel.

For gas control optimization, the on-chip gassing performance was simulated using computational fluid dynamics with experimentally determined gas-inflow concentration profiles resulting from interconnected mass flow controllers. Therefore, the O_2 concentration was measured inside the supply tubing outlet under different gas-supply flow rates (100, 300, 600 mL/min), when no chip was installed (Fig. 2C). This was necessary because likely dead volumes in the mass flow controller setup were affecting the resulting switching performance, mostly when O_2 flow was fully switched off and residual O_2 remained inside the non-perfused tubing and connectors. The residual O_2 was depleted relatively slowly by diffusion and delayed on-chip switching performance. When switching to higher O_2 levels, this problem was not observed, since all interconnections were continuously perfused and no controller was switched off. As depicted in Fig. 2C, the simulated O_2 level in the fluid channel exhibits a corresponding change from 21% to 0% when the O_2 level in the inlet gas is changed from 21% O_2 to 0% O_2 at $t = 0$ min. The

simulation results indicated that the gas-supply volume flow rate, was the limiting factor in our design, mostly impacting the exchange time of O_2 in the fluid channel, rather than diffusion across the PDMS membrane. Based on the simulation results, the maximum total flow rate of N_2 and O_2 at 600 mL/min was applied to achieve rapid modulation of O_2 within the fluid channel.

With the determined total flow rate, the O_2 switching performance was experimentally validated by imaging the fluorescence lifetime of the O_2-sensitive dye (tris(2,2'-bipyridyl)dichlororuthenium(II)hexahydrate, RTDP) inside the fluid channel with FLIM. Figure 2D depicts O_2 concentration measured in the fluid channel after the gas exchange from 21% to 0% and vice versa. The supply gas diffused into the fluid rapidly, achieving 99% of the aimed conditions (corresponding to a residual O_2 concentration of 0.21% when switching from 21% to 0%) within 15 seconds in both switching directions. The O_2 level in the gas supply was also switched between 21% and 0% at various oscillation half-periods T' (T' = 60, 30, 10, 5, 2, 1, 0.5 min), showing the robust experimental O_2-level data when toggling between 21% and 0% at various T', as shown in Fig. S1. These device characterization results ensure a fast gas exchange in the order of seconds in the developed microfluidic device.

E. coli growth in constant and homogeneous O_2 environments

The fabricated double-layer cultivation device was first employed to cultivate *E. coli* MG1655 under a range of constant O_2 levels, between 0% and 21%, to determine whether the impact of various O_2 levels on microbial growth can be spatiotemporally resolved at the single-cell level. *E. coli* is a facultative anaerobic bacterium that can grow under aerobic, microaerobic, and anaerobic conditions. As known, the O_2-limited growth is slower compared to the growth under O_2-rich environments[18].

Fig. 3A and B show representative time series of phase contrast images of *E. coli* cultivated under aerobic (21% O_2) and anaerobic (0% O_2) conditions. Both cultivations started with a single cell at 00:00 h, with a resulting larger colony area at 21% O_2 after 03:00 h cultivation time.

To further investigate whether various O_2 concentrations also result in a corresponding decrease in cell growth in the microfluidic growth chambers, we cultured *E. coli* under constant O_2 concentrations, at 0%, 0.1%, 0.5%, 1%, 5%, 10%, and 21% O_2 in separate experiments. As shown in Fig. 3C, the colony areas (A_{colony}), the sum of the individual cell areas, are quantified from the phase contrast time-lapse images. As

5/33

evident from the plot, A_{colony} exhibits exponential growth, with the lowest rate being observed at 0% O_2.

In Fig. 3D, the exponential growth rates μ were quantified based on A_{colony} in the exponential growth phase, showing comparable growth at O_2 concentrations between 21% and 1%. Conversely, μ strongly decreases when the O_2 level is below 0.5%. The low K_{O_2} value of 0.07 from the adapted Monod kinetic model also indicates a strong decrease in growth rate at very low O_2 levels. These results indicate that an O_2 concentration of at least below 0.5% is required to observe a measurable change in the growth rate of *E. coli* within our device. Based on the gas exchange characterization shown in Fig. 2D, the minimum switching time, $t_{\min}$, necessary to observe a detectable change between aerobic and anaerobic growth was approximately 15 seconds. This corresponds to an achieved O_2 level of 0.21%.

Beyond colony growth, our data also provide insights at the single-cell level. In Fig. 3E, each gray plot represents the area of an individual cell ($A_{\text{single cell}}$) measured at $t = 2$ h, with red plots representing the mean values. These mean values increase as oxygen concentration rises, which is consistent with the observation that cells with higher growth rates generally exhibit larger sizes[26–28]. Interestingly, $A_{\text{single cell}}$ displayed considerable variation, ranging up to 14 μm^2. This wide distribution suggests cell size heterogeneity within the population, likely reflecting a mixture of cells at different stages: smaller cells immediately post-division, larger cells just before division, and extensively sized cells with fewer division cycles. Such intra-population diversity can be effectively resolved using microfluidic cultivation combined with single-cell, time-lapse imaging.

E. coli growth in periodically oscillating O_2 environments

We then cultivated *E. coli* in oscillating O_2 environments to investigate how these oscillations affect bacterial growth. Experiments were conducted with various oscillation half-periods ($T' = 60, 30, 10, 5, 2$, and 1 min), and the results are presented in Fig. 4A-F (top: A_{colony}, bottom: instantaneous growth rate $\mu_{\Delta t}$). In Fig. 4A (top), the distinct growth rates during aerobic and anaerobic phases for each $T' = 60$ min cycle are observable from A_{colony}. The rate of change in A_{colony} was further quantified by $\mu_{\Delta t}$, calculated as the first derivative of $\ln\left(A_{\text{colony}}\right)$. In Fig. 4A (bottom), a distinctive growth pattern under oscillating conditions emerges, where $\mu_{\Delta t}$ decreases directly after switching from aerobic to anaerobic conditions. A 1.2 fold decrease compared to growth at constant 0% O_2 conditions ($\mu_{0\%} = 1.38 \pm 0.06$ h^{-1}) occurs, followed by

a gradual increase up to around $\mu_{0\%}$. We determined t_{response}, the time to hit the lowest $\mu_{\Delta t}$, and t_{recovery}, the time required to recover up to $\mu_{0\%}$, both counting from the switch from aerobic to anaerobic gassing phase. t_{response} and t_{recovery} are determined to be 1.3 ± 0.1 minutes and 35.2 ± 4.9 minutes, respectively. After t_{recovery}, the growth was stabilized around $\mu_{0\%}$ till the end of the anaerobic gassing phase. After the switch from anaerobic to aerobic gassing phase, in contrast, A_{colony} increased rapidly, reaching the growth rate at constant 21% O_2 concentration ($\mu_{21\%} = 1.95 \pm 0.03$ h^{-1}) within a minute.

At $T' = 30$ min, $\mu_{\Delta t}$ shows a growth tendency similar to $T' = 60$ min, characterized by the steep decrease right after the switch from aerobic to anaerobic conditions, and the following growth recovery till the end of the anaerobic gassing phase, as shown in Fig. 4B. At $T' = 10$, 5, and 2 min, we observe $\mu_{\Delta t}$ hitting the lowest value, and the following gradual recovery phase, but never reaching $\mu_{0\%}$, simply due to insufficient time for recovery and adaptation, as shown in Fig. 4C-E. In the case of $T' = 2$ min, only a brief recovery phase is observed after the response phase. At $T' = 1$ min, the steep decrease after the switch from aerobic to anaerobic conditions is observed without a recovery phase, followed by a fast increase right after the switch from anaerobic to aerobic conditions, as shown in Fig. 4F. As a result, the $\mu_{\Delta t}$ line plots at $T' = 2$ min and 1 min represent simpler waveforms (monotonous up and down), compared to the other cases.

The single-cell area also exhibited a distinct increase under aerobic and anaerobic gassing phases. Figure S2A-F are plotted with $A_{\text{single cell}}$ obtained from individual cells growing in a representative chamber of each oscillation condition. Figure S2 allows us to speculate how individual cells increase their cell size by following neighboring plots, without needing cell tracking that requires more complicated analytical setups. As for overall tendencies, the plots show a faster area increase rate under aerobic than anaerobic gassing phases, similar to colony-area analysis. A rapid increase/decrease in $A_{\text{single cell}}$ was observed immediately after each gassing switch across all oscillation conditions. Notably, a clear recovery in $A_{\text{single cell}}$ was observed when the oscillation half-periods were sufficiently longer than t_{response} ($T' = 60$, 30, and 10 min).

Periodic growth synchronized with applied O_2 oscillations

To compare and examine further the periodic growth behavior induced by different O_2 oscillations, growth data is averaged over periods and plotted over the period fraction, as shown in Fig. 5A. Growth data with more than three periods (T' = 10, 5, 2, and 1 min) were analyzed.

The periodical comparison suggests that $\mu_{\Delta t}$ line plots from T' = 2 and 1 min have simpler waveforms compared to the other T' that are sufficiently longer than $t_{response}$. To examine the waveform complexity of $\mu_{\Delta t}$ line plots at various T', the frequency spectrum of $\mu_{\Delta t}$ line plots were analyzed using the fast Fourier transform (FFT) as shown in Fig. 5B. There are several frequency peaks at T' = 10 and 5 min. These several peaks imply the complicated waveform of $\mu_{\Delta t}$ line plots due to the existence of response and recovery phases. In contrast, there is only one frequency peak at T' = 2 and 1 min. The single peaks imply the simpler $\mu_{\Delta t}$ line plots, representing only the response phase. Notably, the highest peaks from FFT corresponded to applied O_2 oscillation half-periods T', showing that the periodic growth dynamics were synchronized with applied O_2 oscillation periods (T' = 10 min: 7.8×10^{-4} Hz, T' = 5 min: 1.8×10^{-3} Hz, T' = 2 min: 4.1×10^{-3} Hz, T' = 1 min: 8.4×10^{-3} Hz).

Distinct growth behavior dependent on aerobic/anaerobic gassing phases

To further analyze the O_2-oscillation-dependent growth behavior, we determined phase-averaged growth rates under aerobic and anaerobic gassing phases ($\bar{\mu}_{aerobic}$, $\bar{\mu}_{anaerobic}$) by calculating the growth rate for each T', as illustrated in Fig. 6A.

In Fig. 6B, $\bar{\mu}_{aerobic}$ and $\bar{\mu}_{anaerobic}$ for each T' are summarized. At T' = 60 min, $\bar{\mu}_{aerobic}$ and $\bar{\mu}_{anaerobic}$ are comparable to $\mu_{21\%}$ and $\mu_{0\%}$ respectively, indicating the sufficient recovery time and growth stabilization after the gassing phase shift. At T' = 30 and 10 min, $\bar{\mu}_{aerobic}$ is comparable to $\mu_{21\%}$, whereas $\bar{\mu}_{anaerobic}$ is below $\mu_{0\%}$. This is due to insufficient recovery time under the anaerobic phases ($t_{response} < T' < t_{recovery}$), resulting in an overall lower growth rate over anaerobic phases. This trend became more obvious at T' = 5 and 2 min, with lower $\bar{\mu}_{anaerobic}$ because of less time for growth recovery. Interestingly, $\bar{\mu}_{aerobic}$ was higher than $\mu_{21\%}$ at T' = 5 and 2 min. This high $\bar{\mu}_{aerobic}$ is the result of the steep increase in growth rate right after the switch from anaerobic to aerobic gassing phases and insufficient time to adjust the growth rate to around $\mu_{21\%}$, as shown in Fig. 4D and E. Lastly, $\bar{\mu}_{aerobic}$ and $\bar{\mu}_{anaerobic}$ at T' = 1 min were close to

each other, implying the growth adaptation attempt back and forth between aerobic and anaerobic phases, although insufficient time to adapt to either of gassing phases ($T' < t_{\text{response}}$). These results demonstrate a phase- and oscillation-period-dependent growth behavior that can be classified into several cases by growth characteristic values, t_{response} and t_{recovery}.

Furthermore, we investigated the difference in phase-averaged growth rate over periods to examine the growth robustness under repeated O_2 oscillations. Growth data with more than 3 periods were analyzed ($T' = 10, 5, 2,$ and 1 min). As shown in Fig. 6C, $\bar{\mu}_{\text{aerobic}}$ and $\bar{\mu}_{\text{anaerobic}}$ plotted over periods exhibit robust and steady trends, even with repetitive 60 periods at $T' = 1$ min. This result indicates the versatility of the developed platform to stably create O_2 oscillating conditions and analyze microbial growth under such conditions.

Discussion

The objective of this study was to investigate the growth dynamics of *E. coli* under oscillating O_2 environments. Previous research on microbial growth response to gaseous changes has been extensively conducted, but predominantly focused on single shifts in O_2 availability. This restriction has resulted in our limited understanding of microbial growth response to O_2 fluctuations. To facilitate further investigation, we developed the double-layer microfluidic platform for the time-lapse monitoring of microbes under rapidly oscillating O_2 environments. The platform enabled the cultivation of microbes under well-defined on-chip O_2 oscillating environments and simultaneous observation of microbial behavior at high spatiotemporal resolution. Our platform enabled the thorough analysis of the growth dynamics of *E. coli* based on growth rates in different time scales ($\mu, \bar{\mu}, \mu_{\Delta t}$). While single-cell analysis is known for its high workload required to extract biological information such as growth rates at the single-cell level, it turned out to be crucial to establish fully automated image analysis and data extraction prior to the development of the microfluidic device. Based on these analysis procedures, we quickly iterated and adapted our microfluidic chip prototypes and directly verified the effects based on the biological outputs with only overnight delay. This high walkaway time and high throughput experimentation allowed us to primarily focus on optimizing the microfluidic chip design and experiment preparation, while biological insights were automatically extracted. Such a single-cell analysis of continuous microbial growth under oscillating

O₂ environments with high temporal resolution was impossible with conventional analytical platforms.

The thorough growth analysis presented here demonstrates distinct growth dynamics induced by O_2 oscillations, which are characterized by an immediate decrease in $\mu_{\Delta t}$ after the switch from aerobic to anaerobic gassing phases (response), followed by gradual increase (recovery), and later stabilized state. These distinguished cell behaviors occur depending on oscillation half-periods T'. This is reasonable, considering that all the cellular events associated with environmental change occur at different timescales. For example, the O_2 oscillation with $T' = 1$ min was sufficient to rapidly and strongly decrease the *E. coli* growth rates in the respective anaerobic gassing phase (Fig. 4F). This observation could be explained by the rapid depletion of the ATP pool under O_2 limitation, which occurs within the time scale of microbial responses to environmental fluctuations associated with enzymatic reactions and metabolite turnover[22]. A recurring increase in the *E. coli* growth rates were observed when $T' > t_{\text{response}}$ (Fig. 4A-D). This adaptation to prolonged anaerobic phases is most likely the result of specific regulatory processes that alter gene expression patterns, leading to a gradual change in cell metabolism[21]. Under the switch from anaerobic to aerobic gassing phases, the initial peak and the subsequent gradual decrease of $\mu_{\Delta t}$ was also observed. This temporal change in growth rate may be attributed to transient accumulation or excretion of metabolites as a result of maintaining homeostasis upon the gaseous transition[19,29]. The FFT and phase-averaged growth rate analyses revealed periodic and robust growth dynamics synchronized with the applied O_2 oscillation periods. This result implies the cellular capability to respond and adapt to corresponding extracellular O_2 environments and highlights the importance of O_2 in determining cellular growth behavior.

The demonstrated experiment and analysis platform can be strengthened more with further improvements. The O_2 measurement with FLIM and the O_2-sensitive dye requires two-point calibration at known O_2 availability. This calibration was done by flushing synthetic air containing either 0% or 21% of O_2. While controlling the O_2 availability to 21% was credible, achieving a strict O_2 control at 0% remained challenging due to potential disturbances from high air permeability and the possibility of residual air remaining within the PDMS. By improving the calibration method to ensure strict 0% O_2 availability, such as by using chemical O_2 scavengers[30–32] compatible with the O_2-sensitive chemical, more precise on-chip O_2 control under anaerobic conditions may be possible to achieve.

The developed device and the finding regarding microbial behavior under O_2 oscillation have the potential to be applied to a wide range of research fields. In terms of practical applications, the findings are useful in characterizing and improving industrial bioprocesses. The fluctuating environments resulting from conditional heterogeneity in large-scale bioreactors have been widely reported, which result in unexpected inefficiency and yield losses[9–11]. To address this issue, it is of the utmost importance to gain a further understanding of microbial behavior under fluctuating environments. The developed device provides an on-chip environment that mimics rapid O_2 fluctuations inside bioreactors. This enables the analysis of O_2 fluctuation-specific microbial behavior, including the emerging phenotypic heterogeneity at single-cell resolution, which was previously not possible.

A comparable approach to recreate fluctuating O_2 environments and live-cell imaging could also prove beneficial in fundamental biology and biomedicine, such as investigating the interaction of gastrointestinal host cells and microbial communities under fluctuating O_2 environments. There has been growing evidence that O_2 dynamics play a pivotal role in maintaining intestinal homeostasis[33, 34]. The intricate regulatory mechanisms at the interface of host cells and the microbiome, and the role of O_2 are of great interest since these interactions are linked to various diseases[34]. Moreover, several reports imply the existence of O_2 fluctuations in the intestine and the intestinal epithelial-microbiome interface that arise from periodic ingestion of nutrients or intermittent changes in O_2 availability in the blood[35–37]. The presented device and analysis could be applied to study the interplay between host epithelial cells and microbiomes by emulating such an O_2 fluctuating environment.

Materials and Methods

Microfluidic device fabrication

The double-layer microfluidic device, comprising an upper and a lower layer, was fabricated by molding PDMS in separate molds and by assembling (Fig. 2A)[38]. Firstly, the mold for the upper layer was prepared by 3D printing with stereolithography (Form 3B, Formlabs, US). The mold was filled with a mixture of pre-cured PDMS solution (10:1) and heated to 80°C for 20 minutes to initiate the first curing step. A silicon wafer with a two-layer SU-8 photoresist was fabricated by photolithography as described in a previous paper[39] at Helmholtz Nano Facility, Germany[40] and employed as the mold for the lower layer.

The PDMS was spin-coated onto the SU-8 mold at 1000 rpm for 60 seconds (SPIN150i, APT Automation, Germany) and subsequently heated at 80°C for 10 minutes to initiate the first curing step. Then, the upper layer was peeled off from the mold, cut into chips, and inlets were punched (punching tool $\phi = 0.75$ mm, World Precision Instruments, US). The lower layer was not peeled off at this step. The upper layer was then placed onto the lower layer and heated at 80°C for a minimum of one hour. This constituted the second curing step, whereby the upper and lower layers were irreversibly bonded together through the full curing process. Once fully cured, the chip was peeled off from the wafer, holes were punched ($\phi = 0.50$ mm, World Precision Instruments, US), and bonded to a glass substrate (D263®Bio, 39.5 mm $\times$ 34.5 mm $\times$ 0.175 mm; Schott AG, Germany) by O_2 plasma treatment for 25 seconds (Femto Plasma Cleaner, Diener Electronics, Germany). The bonded chip was heated at 80°C for one minute to increase the stability of the bonding.

Computational simulations

The gas distribution in the PDMS chip was simulated using a finite element method (COMSOL Multiphysics 6.0, COMSOL). A three-dimensional geometrical model was built comprising three distinct subdomains, a PDMS block, a fluid channel, and a gas channel (Fig. S3). A hexahedral mesh was generated for the fluid channel, while a tetrahedral mesh was generated for the remaining geometry. The physical phenomena of fluid flow and gas flow were numerically analyzed by solving the time-dependent Navier-Stokes equations for laminar and incompressible flow. O_2 transport was determined by diffusion and convection, as well as by the ratios between O_2 concentration and O_2 solubility at the different material boundaries. Further details regarding the simulation setup are described in the Supplementary Materials.

Microscopy

An inverted microscope (Nikon Eclipse Ti-E 2, Nikon, Japan), equipped with a CMOS camera (DS-Qi2, Nikon, Japan) for phase-contrast image acquisition and a FLIM camera (550 kHz frequency domain; pco.flim, PCO AG, Germany), was utilized for the experiments. The FLIM camera was connected to a modulated excitation laser (445 nm, 100 mW; pco.flim laser, Omicron-Laserafe Laserprodukte GmbH, Germany). The microscopy setup was customized with a perfect focus system (PFS, Nikon, Japan) and a temperature incubator (Okolab, Italy) to facilitate automated live-cell imaging during cell cultivation

310 on the microscope. Phase-contrast observation for biological cultivation was conducted with a $100\times$

311 objective (Plan Apo λ Oil, Nikon, Japan). FLIM imaging was conducted with a $20\times$ objective (Plan

312 Apo λ, Nikon, Japan). To perform FLIM, a customized filter cube was used, which was composed of an

313 excitation filter (440/40, F47-440), a long-pass dichroic mirror (495LP, F48-495), and an emission filter

314 (605/70, F47-605). All the filter components were purchased from AHF analysentechnik AG, Germany. A

315 custom-made chip holder was used to mount the chip on the microscope stage. The FLIM was calibrated

316 using a reference fluorescent slide with a known lifetime (lifetime = 3.75 ns, UMM-SFG, Starna Scientific,

317 UK) as a standard. Further details are described in a previously published paper[41].

Gas control and O_2 sensing

319 Three interconnected mass flow controllers were utilized to continuously deliver the synthetic air mixture

320 with the desired concentrations of N_2, O_2, and CO_2 (red-y, Vögtlin Instruments GmbH, Switzerland). For

321 on-chip gas control, the inlet of the gas channel was connected to the mass flow controllers. The desired

322 O_2 concentrations in the gas supply were achieved by automatically adjusting the corresponding volume

323 flow rates for O_2 and N_2 while maintaining the total flow rate constant at 600 mL/min throughout the

324 oscillations. 0.4 mL/min of CO_2 was always added to the synthetic air to facilitate reproducible growth

325 of *E. coli*[42]. A tubing with a low gas permeability (N_2: 1.2 barrer, O_2: 2.2 barrer; Tygon®F-4040-A,

326 Saint-Gobain, France) was used to connect the mass flow controller and the hole on the upper layer of the

327 chip. To measure O_2 concentrations of in-flow coming out of the tubing, a fiber O_2 microsensor was used

328 and inserted directly in the tubing (OXR50, pyroscience, Germany).

329 The O_2 level in the chip was measured by fluorescence lifetime imaging (FLIM) and an O_2-sensitive

330 dye, tris(2,2'-bipyridyl)dichlororuthenium(II)hexahydrate (RTDP). The fluorescence of RTDP is quenched

331 in the presence of O_2, which can be quantified as a change in fluorescence lifetime (τ). The fluorescence

332 quenching is described by the Stern-Volmer equation, as follows.

$$[O_2] = \frac{1}{K_q}\left(\frac{\tau_0}{\tau} - 1\right) \tag{1}$$

333 τ_0 is the fluorescence lifetime under 0% O_2, and K_q is the quenching constant. K_q was derived by a

334 two-point calibration, whereby τ_0 and τ at a known O_2 concentration were measured. Here, τ at 21% O_2

(τ_{21}) was used to derive K_q. The gaseous conditions of 0% and 21% O_2 were set by adjusting the mass flow rate of N_2 and O_2. The parameters were determined from the measurement as follows; $\tau_0 = 481$ ns, $\tau_{21} = 307$ ns, $K_q = 2.71$.

Cell preparation

E. coli MG1655 was stored in a ROTI Store cryo vial (ROTI®Store cryo vial, Carl Roth, Germany). All microbial cultivations were conducted using a lysogeny broth (LB) complex medium, comprising 10 g/L peptone, 5 g/L yeast extract, and 10 g/L NaCl. The pH of the LB medium was adjusted to 7.0 with NaOH, autoclaved at 121°C for 20 minutes, and stored at 4°C. All the aforementioned chemicals were purchased from Carl Roth, Germany. A single bead from the cryo vial was transferred to a 20 mL LB medium in a shaking flask and cultured at 37°C, 150 rpm, for around 16 hours. The subsequent culture was initiated by inoculation from the previous culture, with an initial optical density (OD_{600}) of 0.3 or 0.0001, and cultivated until it reached the exponential growth phase.

Microfluidic cultivation and time-lapse imaging

The inoculation in the microfluidic chip was performed with the cell solution containing exponentially growing cells, with $OD_{600} = 0.5$. The cell solution was introduced into the fluid channel of the chip with a syringe (Omnifix®-F 1 mL, Braun, Germany). Following the successful inoculation, the syringe was replaced with a new one containing a fresh medium. The remaining cells within the channel were then flushed by manually pushing the syringe. The medium was perfused at a constant rate of 100 nL/min using a syringe pump (neMESYS, CETONI, Germany). The chip cultivation continued for three hours before the colony reached the chamber size. The time-lapse imaging was performed, with an image acquisition interval $\Delta t = 1$ min for all the cultivation under constant O_2 environments, and $\Delta t = 10$ seconds for all the cultivation under oscillating O_2 environments.

Image analysis

The acquired FLIM image data in nd2 format was saved as OME.TIFF files and processed using Fiji[43] to measure the lifetime in a rectangular ROI (h 500 pixels $\times$ w 100 pixels). A median filter (pixel size = 5) was employed to remove noise.

The details of the image analysis from cultivation experiments are described in previously published papers[41,44]. Briefly, the acquired image data in nd2 format was exported as TIFF files and pre-processed using Fiji, which included rotation, alignment (Correct 3D Drift[45]), and cropping. The pre-processed TIFF files were then uploaded to an OMERO server[46] for subsequent analysis. For the automated image analysis, we developed Jupyter Notebooks and Python to perform deep-learning-based cell segmentation (Omnipose[47]) followed by filtering artifacts and extracting single-cell sizes. These Jupyter Notebooks are designed for a single time-lapse recording and provide video rendering to guarantee and document sufficient cell segmentation quality. We repeatedly apply the same Jupyter Notebook to all our time-lapse images (scaling analysis), leading to fully automated image processing such that experiment results are obtained overnight. The codes for cell segmentation and analysis are openly available at https://github.com/JuBiotech/Supplement-to-Kasahara-et-al.-2025.

Growth analysis

Colony area, A_{colony}, was normalized by the colony area at the start of cultivation to compare between different chambers and conditions. Exponential growth rates, μ, were quantified based on A_{colony} in the exponential growth phase, as follows.

$$\mu = \frac{\ln A_{\text{colony}, \, t} - \ln A_{\text{colony}, \, t_0}}{t - t_0} \tag{2}$$

The relation of growth rate and O_2 concentration was modeled by a Monod kinetic[48] including a growth offset for anaerobic growth, C (h^{-1}) at 0% O_2, as follows.

$$\mu = \mu' \frac{\%O_2}{K_{O_2} + \%O_2} + C \tag{3}$$

$\mu' + C$ (h^{-1}) is the growth rate under high O_2 availability, and K_{O_2} is the so-called Michaelis-Menten constant.

Instantaneous growth rates, $\mu_{\Delta t}$, the first derivative of A_{colony}, were calculated as follows.

$$\mu_{\Delta t} = \frac{\ln A_{\text{colony}, \, t+\Delta t} - \ln A_{\text{colony}, \, t-\Delta t}}{2\Delta t} \tag{4}$$

15/33

Phase-averaged growth rates under aerobic and anaerobic gassing phases ($\bar{\mu}_{\text{aerobic}}$ and $\bar{\mu}_{\text{anaerobic}}$), were determined by averaging obtained values from all the periods in all the analyzed colonies. t_{response} was determined as the time to hit the lowest $\mu_{\Delta t}$. t_{recovery} was determined as the time for the linear regression slope of $\mu_{\Delta t}$ in a shrinking window to reach zero.

The fast Fourier transform (FFT) was performed using the Data Analysis Tools in Excel. The sample size was adjusted to 2^n prior to FFT. For all the growth analysis, growth data between $0\ \text{h} \leq t < 1\ \text{h}$ were omitted since growth data at the beginning of the cultivation was occasionally affected by high noise due to a low initial cell number. Datasets with $\Delta t = 10$ seconds were smoothed by a centered moving average (window size = 5) before calculating $\mu_{\Delta t}$ and the derivative of $A_{\text{single cell}}$, to reduce noise.

Conflict of interest

The authors declare that the research was conducted in the absence of any commercial or financial relationships that could be construed as a potential conflict of interest.

Acknowledgements

Author contributions

K.K. and D.K. designed the study. K.K. conducted the experiments and data analyses. K.K., T.D., and D.K. interpreted the results. J.S. and K.N. contributed to the automated image workflows and data management.

B.S. and E.L. conducted the numerical simulation. K.K., T.D., and D.K. wrote the paper. All authors contributed to the article and approved the submitted version.

Supplementary material

The supplementary material for this article is available.

Data availability statement

The codes for image analysis will be available at https://github.com/JuBiotech/Suppl [ement-to-Kasahara-et-al.-2025](https://github.com/JuBiotech/Supplement-to-Kasahara-et-al.-2025). Microscopy image data will be available at https://doi.org/10.5281/zenodo.13982747.

References

1. Lalejini, A., Ferguson, A. J., Grant, N. A. & Ofria, C. Adaptive phenotypic plasticity stabilizes evolution in fluctuating environments. *Front. Ecol. Evol.* **9** (2021).

2. Fusi, M. *et al.* Ideas and perspectives: The fluctuating nature of oxygen shapes the ecology of aquatic habitats and their biogeochemical cycles – the aquatic oxyscape. *Biogeosciences* **20**, 3509–3521 (2023).

3. Stocker, R. Marine microbes see a sea of gradients. *Science* **338**, 628–633 (2012).

4. Dedrick, S. *et al.* Impact of temporal pH fluctuations on the coexistence of nasal bacteria in an in silico community. *Front. Microbiol.* **12**, 613109 (2021).

5. Zhang, Y. *et al.* Temperature fluctuation promotes the thermal adaptation of soil microbial respiration. *Nature Ecology & Evolution* **7**, 205–213 (2023).

6. Cohen Susan E. & Golden Susan S. Circadian rhythms in cyanobacteria. *Microbiol. Mol. Biol. Rev.* **79**, 373–385 (2015).

7. Formenti, F. *et al.* Respiratory oscillations in alveolar oxygen tension measured in arterial blood. *Sci. Rep.* **7**, 1–10 (2017).

8. Lozupone, C. A., Stombaugh, J. I., Gordon, J. I., Jansson, J. K. & Knight, R. Diversity, stability and resilience of the human gut microbiota. *Nature* **489**, 220–230 (2012).

9. Enfors, S. O. *et al.* Physiological responses to mixing in large scale bioreactors. *J. Biotechnol.* **85**, 175–185 (2001).

10. Takors, R. Scale-up of microbial processes: Impacts, tools and open questions. *J. Biotechnol.* **160**, 3–9 (2012).

11. Bisgaard, J. *et al.* Characterization of mixing performance in bioreactors using flow-following sensor devices. *Chem. Eng. Res. Des.* **174**, 471–485 (2021).

12. Miethke, M. & Marahiel, M. A. Siderophore-based iron acquisition and pathogen control. *Microbiol. Mol. Biol. Rev.* **71**, 413–451 (2007).

13. Cabiscol, E., Tamarit, J. & Ros, J. Oxidative stress in bacteria and protein damage by reactive oxygen species. *Int. Microbiol.* **3**, 3–8 (2000).

14. André, A. C., Debande, L. & Marteyn, B. S. The selective advantage of facultative anaerobes relies on their unique ability to cope with changing oxygen levels during infection. *Cell. Microbiol.* **23**, e13338 (2021).

15. Martín-Rodríguez, A. J. Respiration-induced biofilm formation as a driver for bacterial niche colonization. *Trends Microbiol.* (2022).

16. Partridge, J. D., Scott, C., Tang, Y., Poole, R. K. & Green, J. *Escherichia coli* transcriptome dynamics during the transition from anaerobic to aerobic conditions. *J. Biol. Chem.* **281**, 27806–27815 (2006).

17. Ren, T. *et al.* Oxygen sensing regulation mechanism of thauera bacteria in simultaneous nitrogen and phosphorus removal process. *J. Clean. Prod.* **434**, 140332 (2024).

18. Murashko, O. N. & Lin-Chao, S. *Escherichia coli* responds to environmental changes using enolasic degradosomes and stabilized DicF sRNA to alter cellular morphology. *Proceedings National Academy Sciences* **114**, E8025–E8034 (2017).

19. Yasid, N. A., Rolfe, M. D., Green, J. & Williamson, M. P. Homeostasis of metabolites in *Escherichia coli* on transition from anaerobic to aerobic conditions and the transient secretion of pyruvate. *R Soc Open Sci* **3**, 160187 (2016).

20. von Wulffen, J., RecogNice-Team, Sawodny, O. & Feuer, R. Transition of an anaerobic *Escherichia coli* culture to aerobiosis: Balancing mRNA and protein levels in a Demand-Directed dynamic flux balance analysis. *PLoS One* **11**, e0158711 (2016).

21. Pedraz, L., Blanco-Cabra, N. & Torrents, E. Gradual adaptation of facultative anaerobic pathogens to microaerobic and anaerobic conditions. *FASEB J.* **34**, 2912–2928 (2020).

22. Nguyen, J., Lara-Gutiérrez, J. & Stocker, R. Environmental fluctuations and their effects on microbial communities, populations and individuals. *FEMS Microbiol. Rev.* **45** (2021).

23. Nguyen, J. *et al.* A distinct growth physiology enhances bacterial growth under rapid nutrient fluctuations. *Nat. Commun.* **12**, 3662 (2021).

24. Täuber, S., Golze, C., Ho, P., von Lieres, E. & Grünberger, A. dMSCC: a microfluidic platform for microbial single-cell cultivation of *Corynebacterium glutamicum* under dynamic environmental medium conditions. *Lab Chip* **20**, 4442–4455 (2020).

25. Tang, Q. *et al.* Microfluidic-based spatiotemporal control of oxygen concentration in bacteria suspension culture from bulk to the single cells. *Nano Today* **54**, 102067 (2024).

26. Schaechter, M., Maaloe, O. & Kjeldgaard, N. O. Dependency on medium and temperature of cell size and chemical composition during balanced grown of *Salmonella typhimurium. J. Gen. Microbiol.* **19**, 592–606 (1958).

27. Taheri-Araghi, S. *et al.* Cell-Size control and homeostasis in bacteria. *Curr. Biol.* **25**, 385–391 (2015).

28. Bertaux, F., von Kügelgen, J., Marguerat, S. & Shahrezaei, V. A bacterial size law revealed by a coarse-grained model of cell physiology. *PLoS Comput. Biol.* **16**, e1008245 (2020).

29. Beauchene, N. A. *et al.* O_2 availability impacts iron homeostasis in *Escherichia coli. Proc. Natl. Acad. Sci. U. S. A.* **114**, 12261–12266 (2017).

30. Sun, W. *et al.* Interaction study of cancer cells and fibroblasts on a spatially confined oxygen gradient microfluidic chip to investigate the tumor microenvironment. *Analyst* **143**, 5431–5437 (2018).

31. Wang, W., Li, L., Ding, M., Luo, G. & Liang, Q. A microfluidic hydrogel chip with orthogonal dual gradients of matrix stiffness and oxygen for cytotoxicity test. *Biochip J.* **12**, 93–101 (2018).

32. Wu, H. M. *et al.* Widefield frequency domain fluorescence lifetime imaging microscopy (FD-FLIM) for accurate measurement of oxygen gradients within microfluidic devices. *Analyst* **144**, 3494–3504 (2019).

33. Henson, M. A. & Phalak, P. Microbiota dysbiosis in inflammatory bowel diseases: in silico investigation of the oxygen hypothesis. *BMC Syst. Biol.* **11**, 145 (2017).

34. Singhal, R. & Shah, Y. M. Oxygen battle in the gut: Hypoxia and hypoxia-inducible factors in metabolic and inflammatory responses in the intestine. *J. Biol. Chem.* **295**, 10493–10505 (2020).

35. Ward, J. B. J., Keely, S. J. & Keely, S. J. Oxygen in the regulation of intestinal epithelial transport. *J. Physiol.* **592**, 2473–2489 (2014).

36. Zheng, L., Kelly, C. J. & Colgan, S. P. Physiologic hypoxia and oxygen homeostasis in the healthy intestine. a review in the theme: Cellular responses to hypoxia. *Am. J. Physiol. Cell Physiol.* **309**, C350–60 (2015).

37. Moreno-Indias, I. *et al.* Intermittent hypoxia alters gut microbiota diversity in a mouse model of sleep apnoea. *Eur. Respir. J.* **45**, 1055–1065 (2015).

38. Polinkovsky, M., Gutierrez, E., Levchenko, A. & Groisman, A. Fine temporal control of the medium gas content and acidity and on-chip generation of series of oxygen concentrations for cell cultures. *Lab Chip* **9**, 1073–1084 (2009).

39. Grünberger, A. *et al.* A disposable picolitre bioreactor for cultivation and investigation of industrially relevant bacteria on the single cell level. *Lab Chip* **12**, 2060–2068 (2012).

40. Albrecht, W., Moers, J. & Hermanns, B. HNF - Helmholtz Nano Facility. *JLSRF* **3**, A112–A112 (2017).

41. Kasahara, K. *et al.* Enabling oxygen-controlled microfluidic cultures for spatiotemporal microbial single-cell analysis. *Front. Microbiol.* **14**, 1198170 (2023).

42. Merlin, C., Masters, M., McAteer, S. & Coulson, A. Why is carbonic anhydrase essential to *Escherichia coli*? *J. Bacteriol.* **185**, 6415–6424 (2003).

43. Schindelin, J. *et al.* Fiji: An open-source platform for biological-image analysis. *Nat. Methods* **9**, 676–682 (2012).

44. Seiffarth, J. *et al.* ObiWan-Microbi: OMERO-based integrated workflow for annotating microbes in the cloud. *SoftwareX* **26**, 101638 (2024).

45. Parslow, A., Cardona, A. & Bryson-Richardson, R. J. Sample drift correction following 4D confocal time-lapse imaging. *J. Vis. Exp.* (2014).

46. Allan, C. *et al.* OMERO: flexible, model-driven data management for experimental biology. *Nat. Methods* **9**, 245–253 (2012).

47. Cutler, K. J. *et al.* Omnipose: a high-precision morphology-independent solution for bacterial cell segmentation. *Nat. Methods* **19**, 1438–1448 (2022).

48. Couvert, O., Divanac'h, M.-L., Lochardet, A., Thuault, D. & Huchet, V. Modelling the effect of oxygen concentration on bacterial growth rates. *Food Microbiol.* **77**, 21–25 (2019).

49. Kim, M.-C., Lam, R. H. W., Thorsen, T. & Asada, H. H. Mathematical analysis of oxygen transfer through polydimethylsiloxane membrane between double layers of cell culture channel and gas chamber in microfluidic oxygenator. *Microfluid. Nanofluidics* **15**, 285–296 (2013).
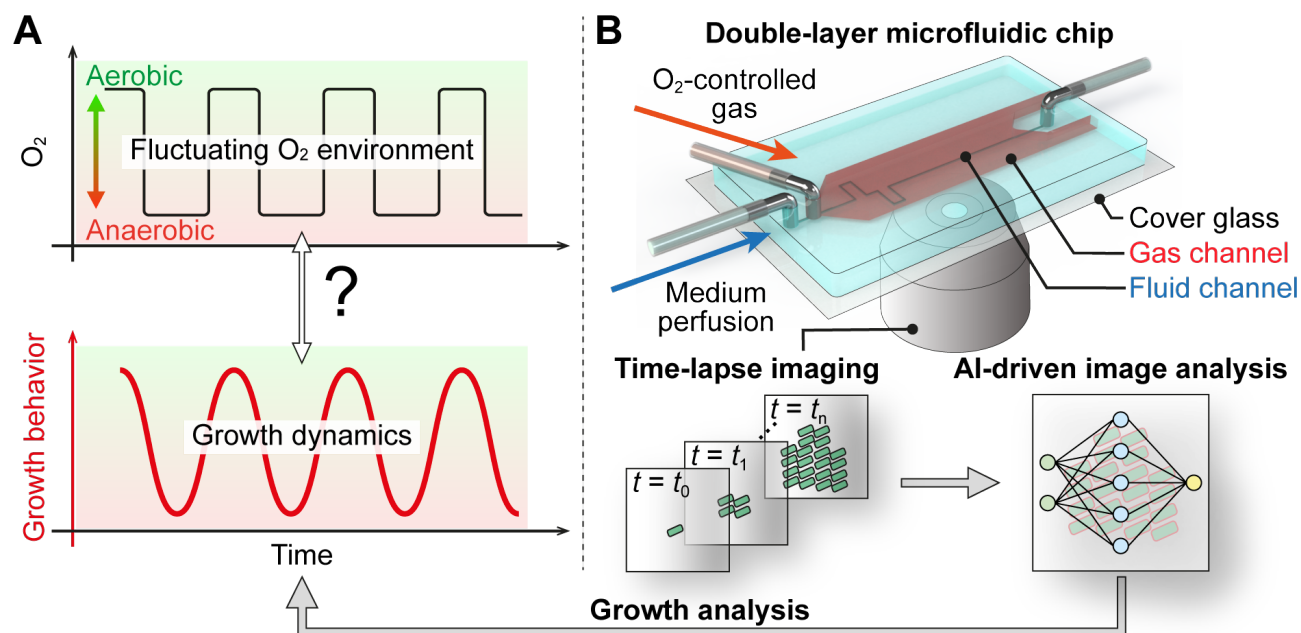
Figure captions

Figure 1. Conceptual illustration of on-chip microbial growth analysis under rapidly oscillating O_2 environments. **(A)** Conceptual sketch of the proposed analysis of microbial growth dynamics in direct correspondence with external oscillating O_2 conditions. **(B)** Analytical platform comprising a double-layer microfluidic chip, time-lapse microscopy, and deep-learning-based image analysis, facilitating high spatiotemporal resolution in characterizing microbial growth under oscillating O_2 environments.
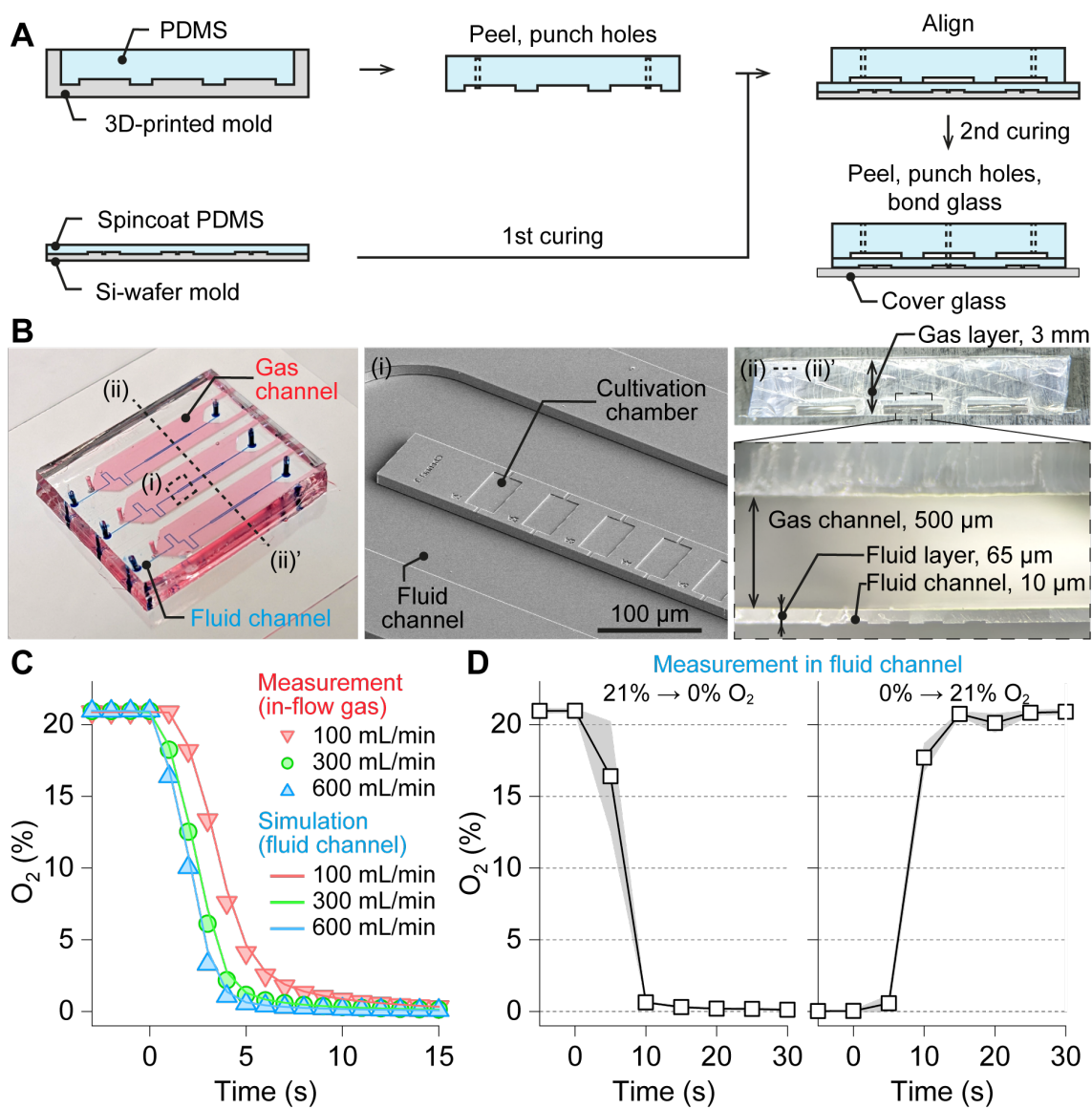
Figure 2. Double-layer PDMS microfluidic chip enabling rapid gas control and single-cell imaging. **(A)** Schematic of the microfluidic chip fabrication process. **(B)** Fabricated microfluidic chip, with (i) an SEM image of the cultivation chambers and (ii) a cross-sectional view. **(C)** Measured O_2 level in the in-flow (plots) and simulated O_2 level at the center of the fluid channel (solid lines) following an O_2 shift from 21% to 0% at mass flow rates of 20, 100, and 600 mL/min. **(D)** Measured O_2 level in the fluid channel following an O_2 shift between 21% and 0%. Data are expressed as mean ± S.D. (n = 3 measurements).
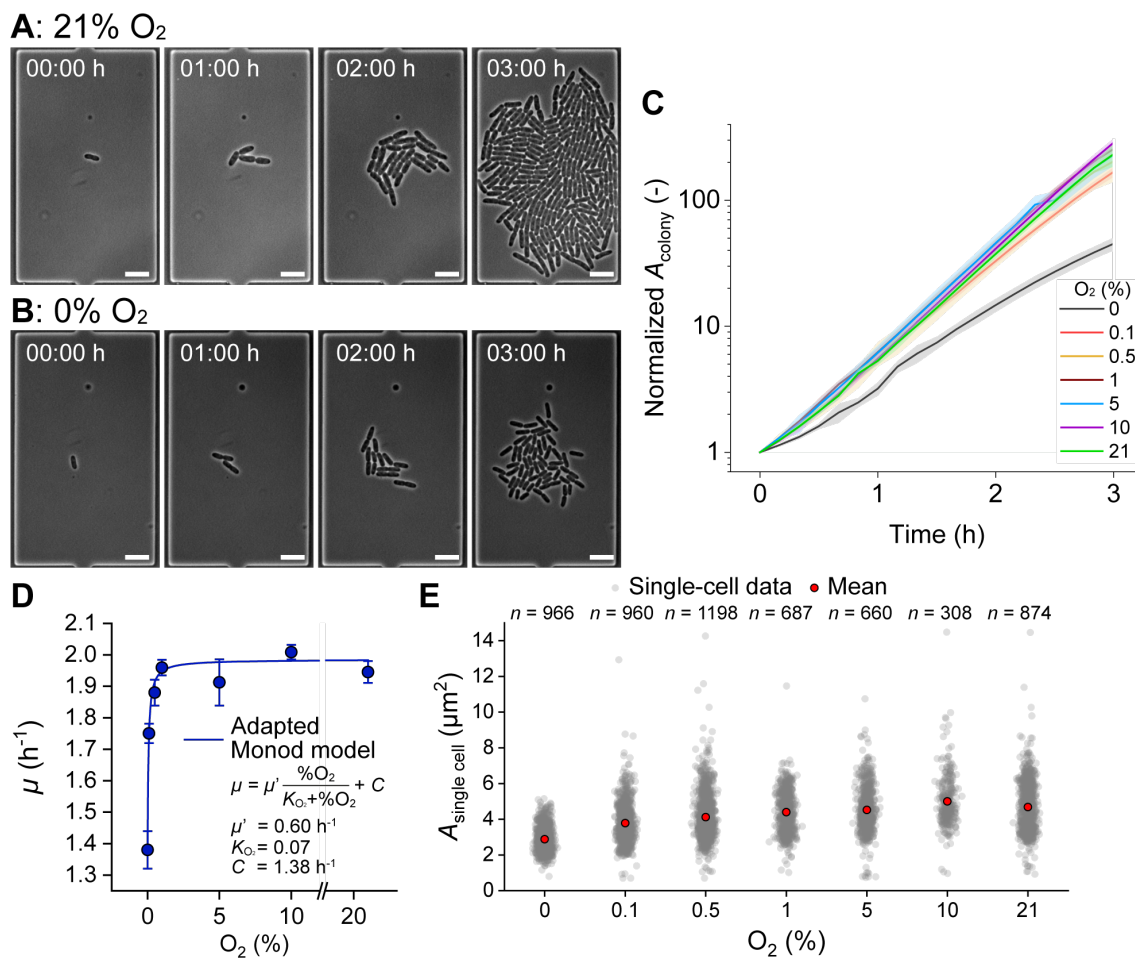
Figure 3. *E. coli* cultivation under steady O_2 conditions. **(A)** Phase-contrast images of *E. coli* cultivated with a 21% O_2 supply (scale bars 5 μm). **(B)** Phase-contrast images of *E. coli* cultivated with a 0% O_2 supply (scale bars 5 μm). **(C)** Growth curves based on colony area (A_{colony}) under various O_2 levels. **(D)** Exponential growth rate (μ) under different O_2 levels, with the adapted Monod kinetic model fit shown by the blue line. **(E)** Single-cell area ($A_{single\ cell}$) across various O_2 levels at $t = 2$ h. Gray dots represent individual cell data, and red dots indicate mean values. The total numbers of analyzed cells are shown in the plot. In **(C)** and **(D)**, data are expressed as mean $\pm$ S.D. $n = 35$ colonies (0%), 27 (0.1%), 21 (0.5%), 16 (1%), 13 (5%), 13 (10%), 29 (21%).
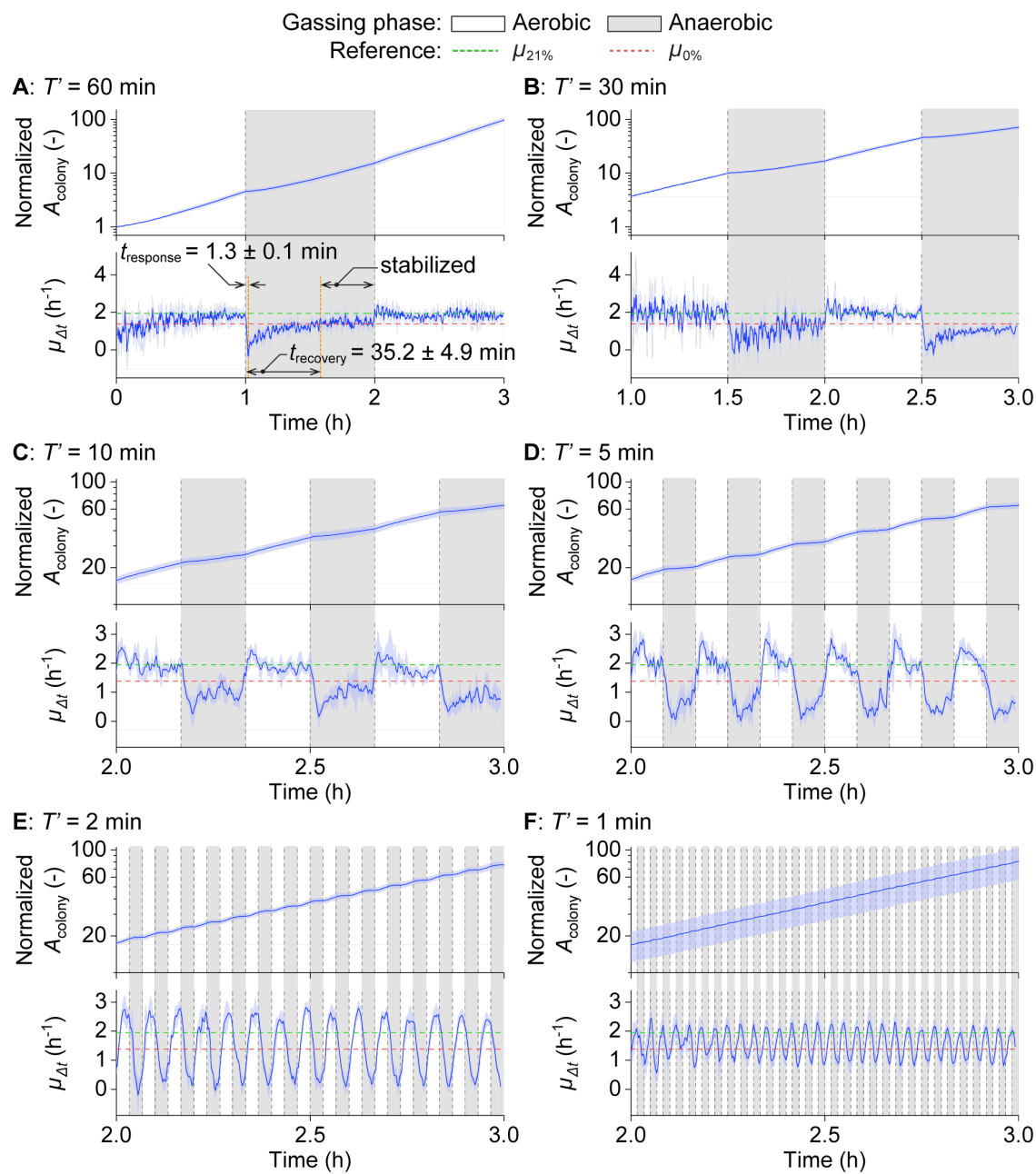
Figure 4. *E. coli* cultivation under oscillating O_2 supplies. **(A - F)** Growth curves based on colony area (A_{colony}, top) and instantaneous growth rate ($\mu_{\Delta t}$, bottom) over time under various oscillation half-periods ($T' = 60, 30, 10, 5, 2,$ and 1 min). Dashed lines represent growth rates under constant 21% ($\mu_{21\%}$) and 0% O_2 ($\mu_{0\%}$) conditions for comparison. Data are expressed as mean $\pm$ S.D. $n = 5$ colonies (60 min), 3 (30 min), 4 (10 min), 4 (5 min), 4 (2 min), 5 (1 min).
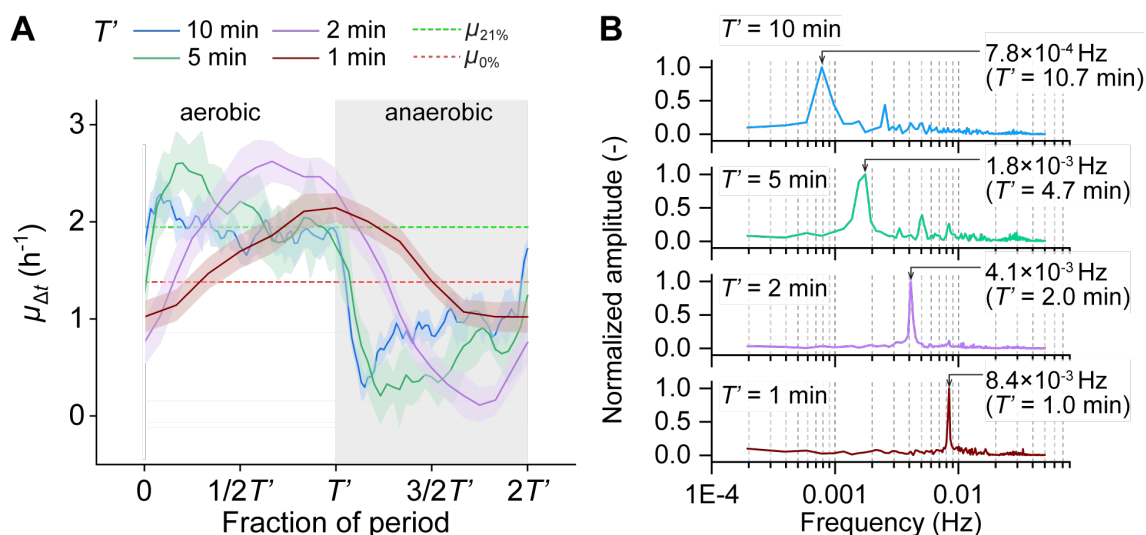
Figure 5. Periodic growth dynamics synchronized with applied O_2 oscillations at various T'. **(A)** $\mu_{\Delta t}$ plotted over fractions of the oscillation period ($2T'$). Data are expressed as mean $\pm$ S.D. across periods. n = 6 (10 min), 12 (5 min), 30 (2 min), 60 (1 min). **(B)** Frequency spectrum of $\mu_{\Delta t}$ at T' = 10, 5, 2, and 1 min, obtained through fast Fourier transform (FFT).
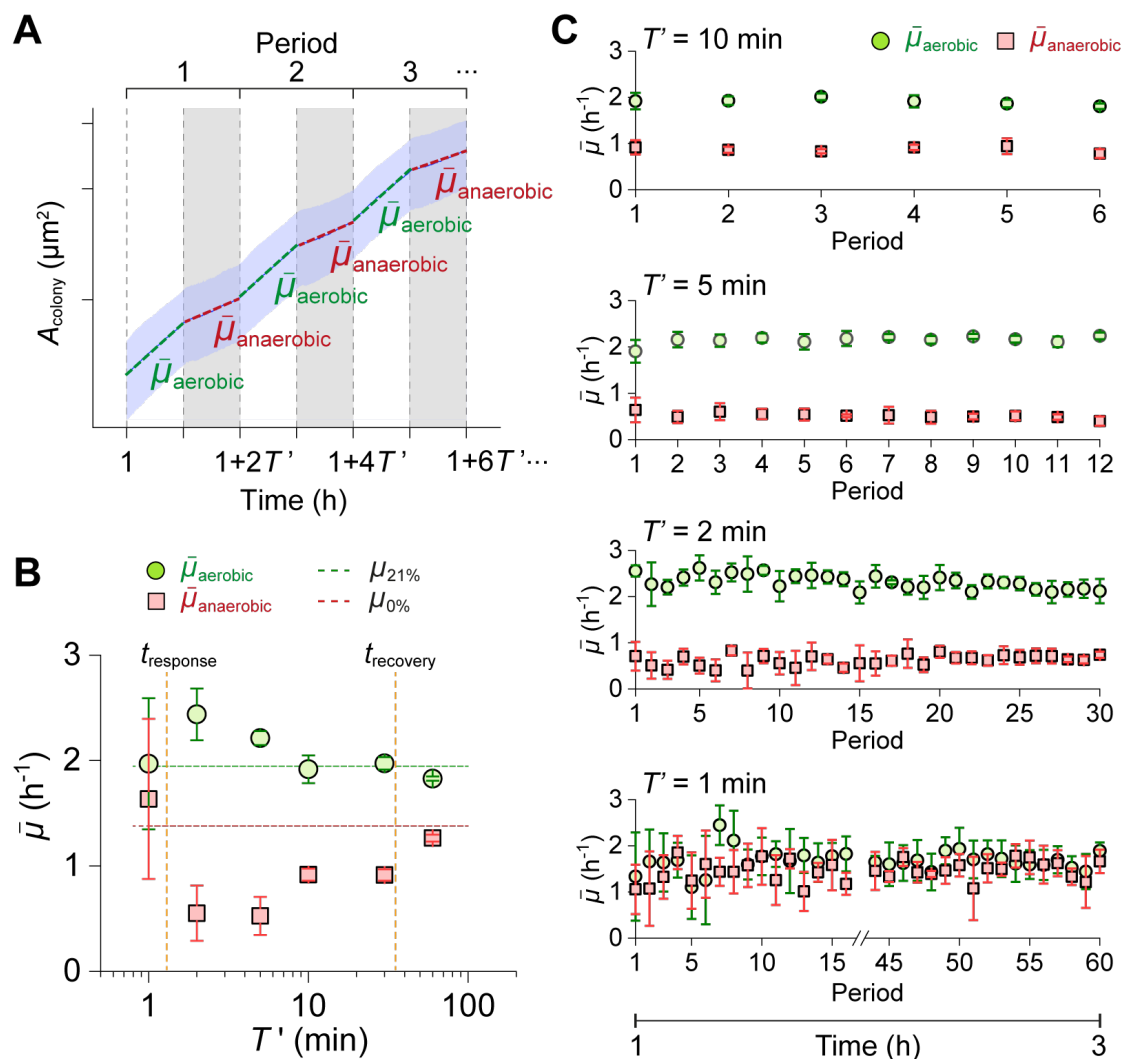
Figure 6. Comparison of phase growth data across different T'. **(A)** Phase-averaged growth rates for each T', calculated for aerobic gassing phases ($\bar{\mu}_{\text{aerobic}}$) and anaerobic gassing phases ($\bar{\mu}_{\text{anaerobic}}$). Dashed lines represent growth rates under constant 21% ($\mu_{21\%}$) and 0% O_2 ($\mu_{0\%}$) conditions for comparison. **(B)** $\bar{\mu}_{\text{aerobic}}$ and $\bar{\mu}_{\text{anaerobic}}$ across different T', with data taken from periods starting at $t = 2$ h. For $T' = 60$ min, growth rate values are taken from half-periods beginning at $t = 1$ h (anaerobic) and 2 h (aerobic). Dashed lines represent growth rates under constant 21% ($\mu_{21\%}$) and 0% O_2 ($\mu_{0\%}$) conditions for comparison. **(C)** Time course of $\bar{\mu}_{\text{aerobic}}$ and $\bar{\mu}_{\text{anaerobic}}$ over multiple periods, illustrating robust growth behavior under oscillatory conditions. Data are expressed as mean $\pm$ S.D. $n = 5$ colonies (60 min), 3 (30 min), 4 (10 min), 4 (5 min), 4 (2 min), 5 (1 min).

Supplementary Materials for:

Unveiling microbial single-cell growth dynamics under rapid periodic oxygen oscillations

Keitaro Kasahara[1,2], Johannes Seiffarth[1,2], Birgit Stute[1], Eric von Lieres[1,2], Thomas Drepper[3], Katharina Nöh[1], and Dietrich Kohlheyer[1,*]

[1]IBG-1: Biotechnology, Institute of Bio- and Geosciences, Forschungszentrum Jülich GmbH, Jülich, Germany

[2]Computational Systems Biotechnology (AVT.CSB), RWTH Aachen University, Aachen, Germany

[3]Institute of Molecular Enzyme Technology, Heinrich Heine University Düsseldorf, Forschungszentrum Jülich GmbH, Jülich, Germany

[*]Corresponding author: IBG-1: Biotechnology, Institute of Bio- and Geosciences, Forschungszentrum Jülich GmbH, 52425 Jülich, Germany. Email: d.kohlheyer@fz-juelich.de
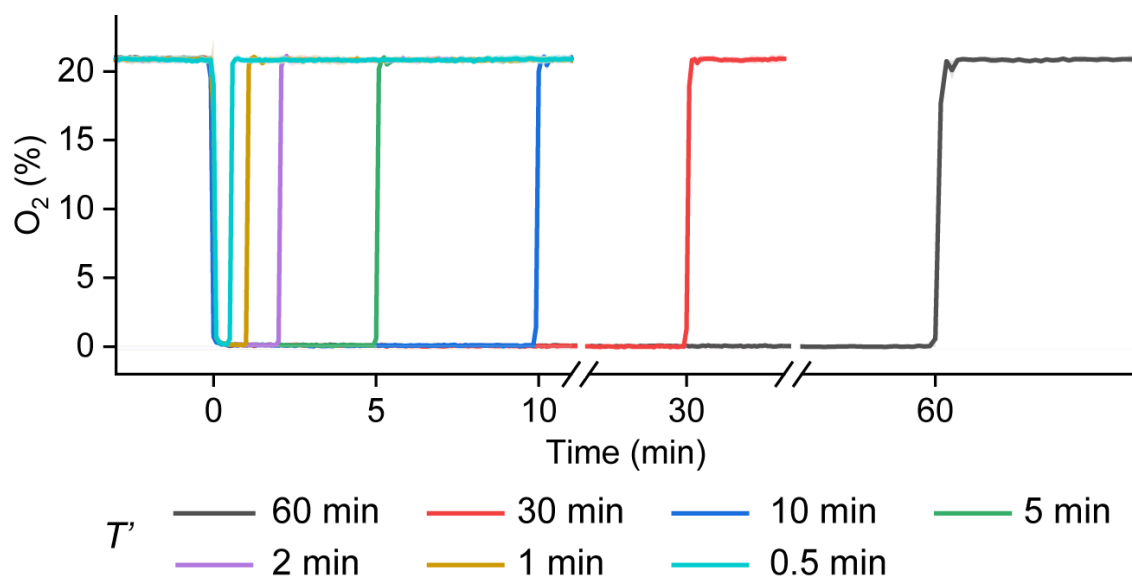
This document includes:

Figure S1. O_2 concentration in the fluid channel of the microfluidic chip determined by RTDP lifetime measurement with FLIM under oscillating O_2 environments at various oscillation half-periods (T').
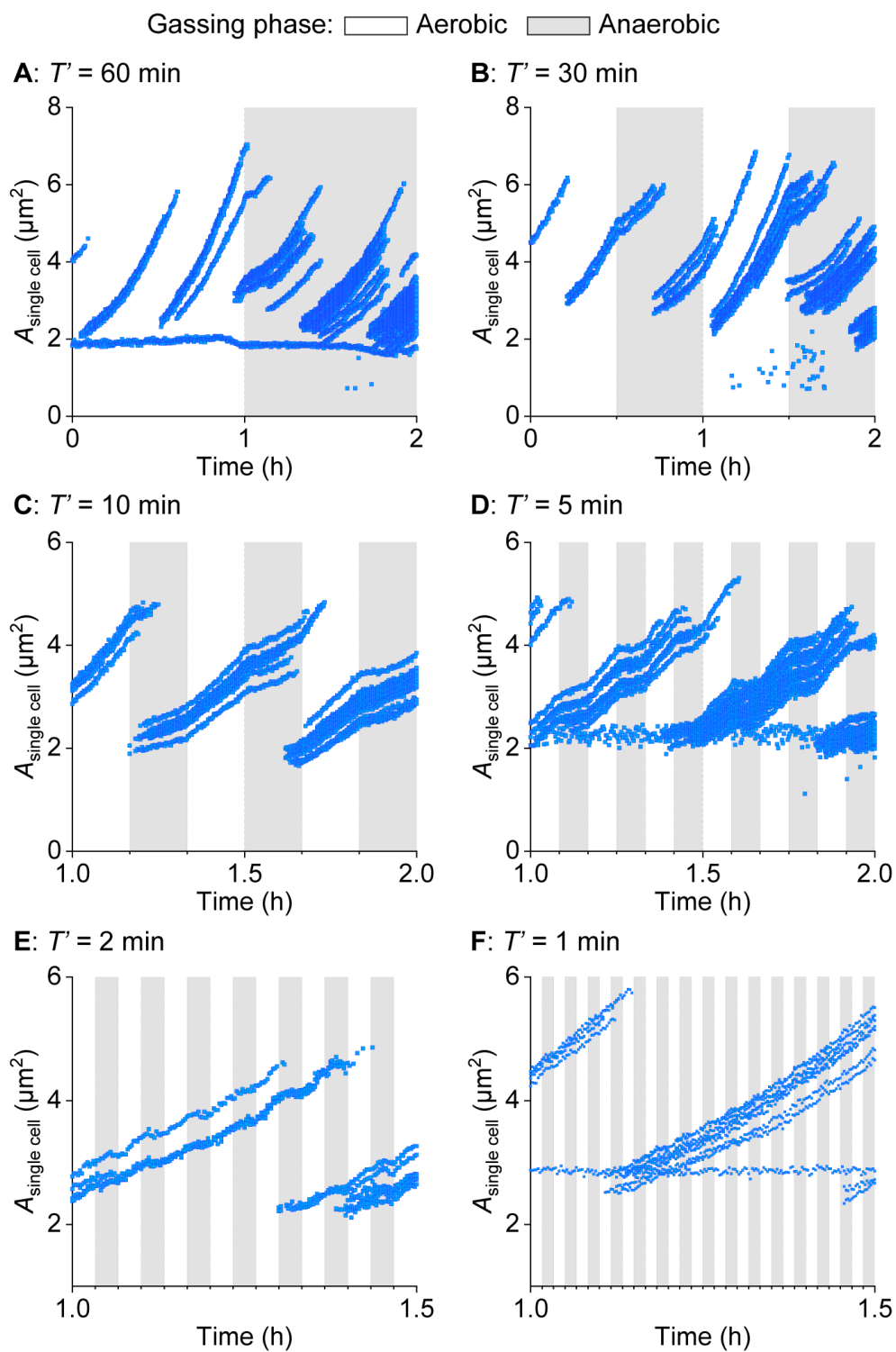
Figure S2. Single-cell area ($A_{\text{singlecell}}$) plotted over time under oscillating O_2 environments at various oscillation half-periods (T').
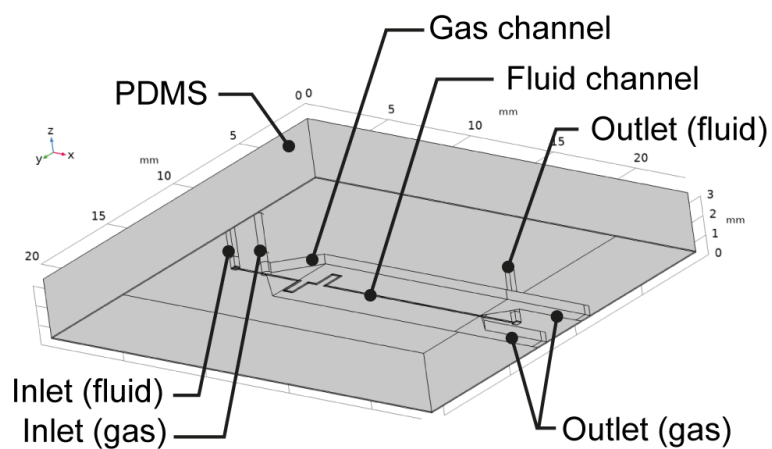
Figure S3. Geometry of the PDMS chip generated for gas diffusion simulation.

Simulation setup

Fluid and gas flow through the respective channels were computed by solving the time-dependent Navier-Stokes equations for laminar, incompressible flow, as follows.

$$\frac{\delta \rho}{\delta t} + \nabla \cdot (\rho\, u) = 0$$

$$\rho \frac{\delta u}{\delta t} + \rho (u \cdot \nabla) u = \nabla \cdot [-\, pI +\, K]$$

$$K = \mu (\nabla u + (\nabla u)^T)$$

Here, ρ represents density (kg/m^3), u is velocity vector (m/s), p denotes pressure (Pa), I is identity matrix, and μ is dynamic viscosity (Pa $\cdot$ s). Boundary conditions at the PDMS block and the glass plane are defined as follows.

$$u = 0 \qquad\qquad\qquad \text{(wall)}$$

$$u = -nU_0 \qquad\qquad\qquad \text{(inlet)}$$

$$[-pI + K]n = -p_0 n \qquad\qquad\qquad \text{(outlet)}$$

n is the boundary normal vector, pointing outward from the domain, and U_0 is the normal inflow speed.

With u defined by the Navier Stokes equations, O_2 transport via convection and diffusion was simulated using the diluted species transport module in COMSOL, incorporating specific boundary conditions as detailed below. The O_2 concentration in the surrounding air is assumed to remain constant at 21%.

$$\nabla \cdot J_i + u \cdot \nabla c_i = R_i$$

$$J_i = -D_i \nabla c_i$$

i is the index for different domains (water, air, PDMS), and D_i represents the diffusion coefficient for each domain i. The velocity u within the PDMS domain is set to 0. c_i denotes the O_2 concentration (mol/m^3) in each domain i, and R describes sources or sinks. Boundary conditions between different domains are

Table S1. Parameters used in simulation (1 atm, 310.15 K)

	water	PDMS	air (21% O_2)	air (100% O_2)
S (mol/m^3)	0.218 [49]	1.25 [49]	8.1375	-
D (m^2/s)	2.7×10^{-9} [49]	7×10^{-9} [49]	2.3×10^{-5}	-
ρ (kg/m^3)	993.31	-	1.1383	1.24
μ (Pa $\cdot$ s)	0.00101	-	1.814×10^{-5}	-

552 defined as follows.

$$\frac{c_i}{S_i} = \frac{c_j}{S_j} \qquad \text{(between PDMS and gas / water channel)}$$

$$c_{\text{PDMS}-\text{air}} = S_{\text{PDMS}} = 1.25 \text{ mol/m}^3 \qquad \text{(between PDMS and surrounding air)}$$

$$-n \cdot J_i = 0 \qquad \text{(at the glass plate)}$$

$$c_{\text{water}-\text{air}} = S_{\text{water}} = 0.218 \text{ mol/m}^3 \qquad \text{(between water and air)}$$

553 S_i represents the solubility of O_2 (mol/m^3) in each domain i at 1 atm and 310.15 K. The initial solubility
554 in air, S_{air}, was calculated to be 8.134 mol/m^3. The parameters used in the simulation were summarized in
555 Table S1.

556 The mesh for the given geometry was generated using a semi-automated approach. First, a hexahedral
557 mesh was created for the fluid channel. The boundaries adjacent to surrounding parts were then converted
558 to a triangular mesh. Finally, the remaining domains were meshed by a tetrahedral mesh with an "extra-
559 fine" resolution.